Laser Physics Letters

LETTER

Effects of Cr^{4+} ions on forming Ince–Gaussian modes in passively Q-switched microchip solid-state lasers

To cite this article: Ming-Ming Zhang *et al* 2019 *Laser Phys. Lett.* **16** 025003

Recent citations

- Structured Light from Lasers
  Andrew Forbes

IOP Publishing | Astro Ltd Laser Physics Letters

Laser Phys. Lett. **16** (2019) 025003 (11pp) https://doi.org/10.1088/1612-202X/aaf791

Letter

Effects of Cr^{4+} ions on forming Ince–Gaussian modes in passively Q-switched microchip solid-state lasers

Ming-Ming Zhang[1], **Sheng-Chuang Bai**[2] **and Jun Dong**[1]

[1] Laboratory of Laser and Applied Photonics (LLAP), Department of Electronic Engineering, College of Electronic Science and Technology, Xiamen University, Xiamen 361005, People's Republic of China
[2] Department of Automation, Tsinghua University, Beijing 100084, People's Republic of China

E-mail: jdong@xmu.edu.cn

Received 30 July 2018, revised 27 November 2018
Accepted for publication 1 December 2018
Published 15 January 2019

Abstract

The effects of Cr^{4+} ions on forming Ince–Gaussian (IG) laser modes in a tilted pumped Cr^{4+}:YAG passively Q-switched (PQS) Nd:YAG microchip lasers has been studied experimentally and theoretically. The formation of Cr^{4+}-ion domains in Cr^{4+}:YAG crystal has been proposed based on the spatial distribution of Cr^{4+} ions in Cr^{4+}:YAG crystal. The spatial modulation effect of Cr^{4+}-ion domains on selecting a transverse mode has been investigated based on their periodic distribution and nonlinear absorption of the Cr^{4+} saturable absorber. The formation of IG modes in the Nd:YAG/Cr^{4+}:YAG PQS microchip laser under tilted pumping has been demonstrated theoretically with the spatial modulation of the Cr^{4+}-ion domains in Cr^{4+}:YAG crystal and the inversion population distribution, by taking account of the thermal lens effect. The IG modes selected theoretically in the Nd:YAG/Cr^{4+}:YAG PQS microchip laser are in good agreement with experimentally obtained IG modes. This work provides a theoretical model of the selection of IG modes with Cr^{4+}-ion domains in a tilted beam pumped Nd:YAG/Cr^{4+}:YAG PQS microchip laser to produce efficient, stable and controllable IG laser modes.

Keywords: Ince–Gaussian, microchip laser, passively Q-switched laser, Cr^{4+}:YAG

(Some figures may appear in colour only in the online journal)

1. Introduction

Ince–Gaussian (IG) modes have been demonstrated for potential applications in the optical manipulation of microparticles, optical trapping and investigations into the spatial behavior of phase singularities [1–4]. Laser-diode pumped IG mode solid-state lasers have been obtained using the method of breaking the symmetry of the laser cavity [5–7]. However, these solid-state lasers are a continuous wave (CW) operation, their output power is low and the lasers are less efficient owing to the misalignment of the laser cavity. High-order IG modes Cr,Nd:YAG self-Q-switched (SQS) nanosecond microchip lasers with a peak power of over 1 kW have been demonstrated by applying a tilted pump beam [8, 9], and various high-order IG modes have also been obtained in the Cr^{4+}:YAG passively Q-switched (PQS) Nd:YVO_4 microchip laser under the tilted pumping [10]. It has been demonstrated that the tilted pump scheme is an effective method to break the symmetry of the plane-parallel microchip cavity for generating IG mode lasers. However, the generation mechanism of the IG laser modes in SQS and PQS microchip lasers with a plane-parallel cavity is not clear. Usually, the generation mechanism of the high-order transverse mode can be catagorized as follows: phase modulation [11–14], gain control

[15–17] and loss control [18, 19]. The phase modulation requires the use of spatial light modulation devices such as the liquid crystal spatial light modulator [11, 12], the kinoform phase elements [13] and the digital micromirror device [14]. The IG mode can also be obtained in the solid-state laser with a plano-spherical resonator by off-axis pumping, which is a method of gain control [15, 16]; however, this method does not work for microchip lasers with a plane-parallel cavity, because the symmetry of the plane-parallel cavity is not broken under the off-axis pumping. In addition, the laser mode can be changed by controlling the gain distribution inside the laser crystal [20–23]. Loss control is a method of introducing diffraction loss by using opaque lines [18], a cross hair [5] or a spot-defect mirror [19] in the solid-state laser. However, none of these mechanisms can completely explain the generation mechanism of the IG mode in the PQS microchip laser with a plane-parallel cavity. Besides the laser cavity, the pump beam profile and the saturable absorber also affect the oscillation of the transverse laser modes. Various transverse laser modes have been obtained by changing the pumping beam profiles, for example, the Laguerre–Gaussian (LG), Hermite–Gaussian (HG) and IG modes have been obtained in the Nd:YAG PQS microchip laser pumped with different decentered Gaussian beams [21]. The effects of the Cr^{4+}:YAG saturable absorbers on generating transverse laser modes in PQS solid-state lasers have been studied in recent decades [24–27]. It has been found that the saturable absorber Cr^{4+}:YAG crystal has the effect of the beam narrowing; even though the intracavity aperture is larger than the size of the fundamental mode spot, the fundamental mode was still obtained in a PQS Nd:YAG laser [25]. The high-order LG modes were obtained in a PQS Nd:YAG laser with the help of a saturable absorber combined with a suitable intracavity aperture and a phase element in the cavity. There is a significant difference in the laser intensity distribution between the non-Q-switched operation and the PQS operation, which shows that saturable absorber plays an important role in the transverse-mode selection [26]. Four phase-locked Gaussian beams are generated in the Cr^{4+}:YAG PQS laser due to the dynamic mode filter effect of the saturable absorber [27]. However, the exact process of laser mode selection by the Cr^{4+}:YAG saturable absorber is still unclear in the PQS microchip laser with a plane-parallel cavity. Therefore, the generation mechanism of the IG laser modes in the PQS microchip laser is worth investigating.

In this paper, three comparative experiments (I: CW Nd:YAG microchip laser, II: Nd:YAG/Cr^{4+}:YAG PQS microchip laser, III: Cr,Nd:YAG SQS microchip laser) were designed to study the generation mechanism of the IG laser modes in microchip lasers. A single emitter laser diode was used as the pump source, since the rectangular profile from the single emitter laser diode has better mode matching with the IG mode than the circular Gaussian pump beam. The formation of Cr^{4+}-ion domains as a spatial light filter to force IG modes oscillation in the PQS microchip laser were investigated theoretically and a mechanism of formation of IG modes in the PQS microchip laser was proposed based on the interaction between asymmetrical saturated inversion population distribution inside the laser crystal and the mode selection of the nonlinear absorption of Cr^{4+}-ion domains in Cr^{4+}:YAG crystal. The theoretically formed IG modes in the Nd:YAG/Cr^{4+}:YAG PQS microchip laser are in good agreement with experimentally obtained IG modes.

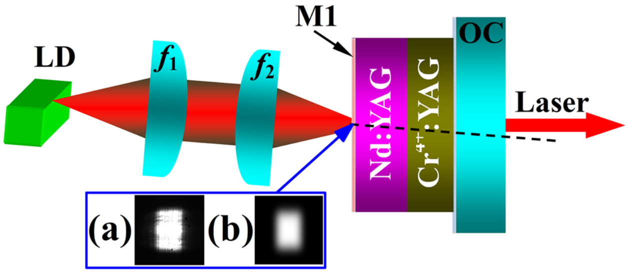

Figure 1. The experimental setup of the tilted beam pumped Cr^{4+}:YAG passively Q-switched Nd:YAG microchip laser for IG mode generation. f_1 and f_2 are the focus lenses with an 8 mm focal length, M1 is the rear cavity mirror, OC is the output coupler. The measured and theoretically calculated pump beam profiles at the focus spot are shown in insets (a) and (b), respectively.

2. Experiments

The experimental setup for studying the mechanism of generating IG modes in the Nd:YAG/Cr^{4+}:YAG PQS microchip laser pumped with a tilted focused beam from a single-emitter laser diode is shown in figure 1. Based on our previous works on direct generation of IG modes in a Cr,Nd:YAG SQS microchip laser under tilted beam pumping [8, 9], by taking into account the exponential decay of the absorbed pump power along the crystal length, the thicknesses of the Nd:YAG crystal and Cr,Nd:YAG crystal were chosen to be 1.8 mm to achieve the same gain in the comparison experiments. The majority of the incident pump power (about 72%) is absorbed by a 1.8 mm thick Nd:YAG crystal or Cr,Nd:YAG crystal doped with 1 at.% Nd^{3+} ions (the absorption coefficient was measured to be $7\,cm^{-1}$ at 808 nm). The extra absorbed pump power by increased crystal length exceeding 1.8 mm is not sufficient to provide gain for laser oscillation. And the losses for the laser are increased by increasing the length of the Cr,Nd:YAG crystal or the Nd:YAG crystal. Therefore, there is a tradeoff for selecting the thickness of the Cr,Nd:YAG or Nd:YAG crystals to achieve high performance of the Cr,Nd:YAG SQS microchip laser or the Nd:YAG/Cr^{4+}:YAG PQS microchip laser. One surface of the Nd:YAG crystal facing pump beam was coated with high reflection (HR) at 1064 nm and antireflection (AR) at 808 nm, and the other surface was coated with AR at 1064 nm to reduce the intracavity loss. A 1.5 mm-thick Cr^{4+}:YAG crystal (0.01 at.% Cr doping concentration) with 95% initial transmission (T_0) was used as a saturable absorber. A 1.8 mm-thick Cr,Nd:YAG SQS crystal codoped with 1 at.% Nd^{3+} ions and 0.01 at.% Cr ions ($T_0 = 94\%$) was used to compare the laser performance with the CW and PQS Nd:YAG microchip lasers. The same Cr doping concentration in Cr^{4+}:YAG and Cr,Nd;YAG crystals was chosen to avoid the effect of Cr^{4+} ion concentration on the formation of the IG mode in PQS microchip lasers. And the small difference between the T_0 of the Cr^{4+}:YAG crystal and the Cr,Nd:YAG crystal can be neglected for the investigation of IG modes in the Nd:YAG/Cr^{4+}:YAG PQS microchip laser and the Cr,Nd:YAG SQS microchip laser. A plane-parallel output coupling mirror with a reflection of 95% at 1064 nm was used in the laser experiments. The cavity length of the CW and Cr,Nd:YAG SQS microchip laser was 1.8 mm, while the cavity length of the Nd:YAG/Cr^{4+}:YAG PQS microchip laser is 3.3 mm. A single-emitter laser-diode working at 808 nm (emitting cross section: $1 \times 50\ \mu m^2$) was used as the pump source. The fast-axis divergence angle of the laser diode was reduced to 10° using a micro lens at the output facet of the laser diode. Two lenses with a focal length of 8 mm were used to collimate and focus the pump beam from the laser diode. The measured footprint at the focused spot was $100\ \mu m \times 150\ \mu m$ (x direction $\times$ y direction) after collimating and focusing optics, as shown in figure 1(a). The pump beam can be described by a super-Gaussian function,

$$E(x, y, z) = E_0 \cdot \exp\left[-\left(\frac{x^4}{w_x(z)^4} + \frac{y^4}{w_y(z)^4}\right)\right], \quad (1)$$

where E_0 is a constant, $w_x(z)$ and $w_y(z)$ are the width of the pump beam along the x-axis and the y-axis at the distance z, respectively. Figure 1(b) gives the theoretically calculated profile of the focused pump beam, which is in good agreement with the experimentally measured pump beam profile, as shown in figure 1(a). The incident pump beam was tilted 3° away from the laser direction for generating IG modes. The characteristics of the laser pulse were recorded using a fast InGaAs photodiode and a digital oscilloscope (Tektronix TDS6604). The output laser beam profiles were monitored and recorded with a laser beam quality analyzer (Thorlabs BC106-VIS).

3. Experimental results

Firstly, the transverse intensity patterns in the CW Nd:YAG microchip laser, the Nd:YAG/Cr^{4+}:YAG PQS microchip laser and the Cr,Nd:YAG SQS microchip laser have been investigated by normal incident to the rectangular pump beam on the crystals. Unfortunately, no IG modes were observed in normally pumped PQS and SQS microchip lasers. The output profiles are fundamental mode or top-hat profiles depending on the applied pump power, which are similar to those obtained in the single-emitter laser diode end-pumped Yb:YAG/Cr^{4+}:YAG PQS microchip laser [28]. The transverse intensity patterns generated in the tilted beam pumped CW Nd:YAG microchip laser, Nd:YAG/Cr^{4+}:YAG PQS microchip laser and Cr,Nd:YAG SQS microchip laser have been measured at different incident pump powers (P_{in}) with a beam profiler. The TEM_{00} mode laser was observed in the CW Nd:YAG microchip laser under tilted beam pumping when the P_{in} was above the pump power threshold (P_{th}) and lower than 1.5 W. The output laser transverse beam profile tends to be a rectangular profile with further increase in P_{in} because the pump power intensity within the rectangular pump beam is sufficient to support multimode laser oscillation. The rectangular transverse intensity profile was maintained with a further increase in the P_{in}, as shown in figure 2(a). The transverse intensity distribution of the laser beam is close to a top-hat profile and no IG modes were observed in the CW Nd:YAG microchip laser within the whole pump power range.

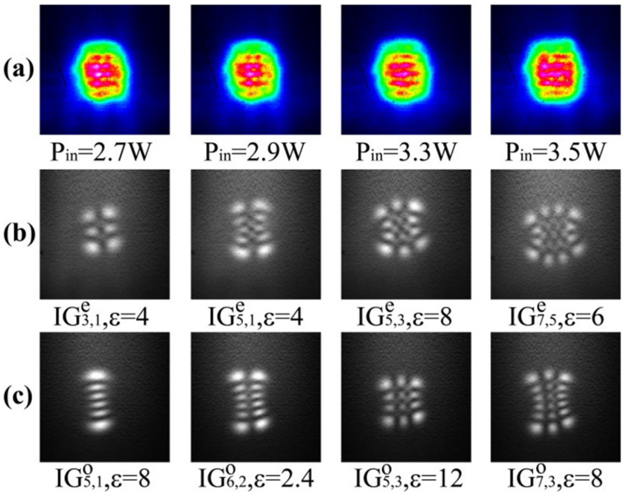

Figure 2. Experimentally obtained laser transverse patterns of (a) CW Nd:YAG microchip laser, (b) Nd:YAG/Cr^{4+}:YAG PQS microchip laser, and (c) Cr,Nd:YAG SQS microchip laser at different incident pump powers.

When the Cr^{4+}:YAG crystal was sandwiched between the Nd:YAG crystal and the output coupler, a Nd:YAG/Cr^{4+}:YAG PQS microchip laser was constructed. The incident pump power threshold increased to 0.8 W owing to the insert loss of the Cr^{4+}:YAG crystal. The TEM_{00} mode laser was observed when the P_{in} was within the range 0.8 W to 1.5 W. The IG modes were observed when the $P_{in} > 1.5$ W. The index of the IG modes increases with the P_{in}. Figure 2(b) gives some typical IG mode distribution obtained in the PQS Nd:YAG microchip laser at different incident pump powers. The top-hat rectangular beam profile of the CW Nd:YAG microchip laser is changed to $IG^e_{3,1}$ ($\varepsilon = 4$) mode for the Nd:YAG/Cr^{4+}:YAG PQS microchip laser at $P_{in} = 2.7$ W. Upon further increase of the P_{in}, the IG mode oscillation was maintained and the index of the IG mode increased. The $IG^e_{5,1}$ ($\varepsilon = 4$) mode was obtained at $P_{in} = 2.9$ W. The Nd:YAG/Cr^{4+}:YAG PQS microchip laser oscillated in $IG^e_{5,3}$ ($\varepsilon = 8$) mode at $P_{in} = 3.3$ W. The $IG^e_{7,5}$ ($\varepsilon = 6$) mode was observed at $P_{in} = 3.5$ W. The similar phenomena of generating IG modes were also observed in the Cr,Nd:YAG SQS microchip laser. The P_{th} increased to 0.92 W for the Cr,Nd:YAG SQS microchip laser, which was attributed to the high intracavity loss induced by codoping Nd^{3+} ions and Cr^{4+} ions in the YAG host crystal. More defects were introduced in the Cr,Nd:YAG crystal because compensation charges such as Ca^{2+} ions or Mg^{2+} ions were needed to form Cr^{4+} ions in the Cr,Nd:YAG crystal. The odd IG modes were obtained in the Cr,Nd:YAG SQS microchip laser when P_{in} was higher than 2 W. Figure 2(c) gives some typical transverse mode distribution obtained in the Cr,Nd:YAG SQS microchip laser at different P_{in}s. Owing to more loss being introduced in the Cr,Nd:YAG crystal, the transverse profiles of the observed IG modes were totally different from those observed in the Nd:YAG/Cr^{4+}:YAG PQS microchip laser at the same P_{in}.

The $\mathrm{IG}^{\mathrm{o}}_{5,1}$ ($\varepsilon = 8$), $\mathrm{IG}^{\mathrm{o}}_{6,2}$ ($\varepsilon = 2.4$), $\mathrm{IG}^{\mathrm{o}}_{5,3}$ ($\varepsilon = 12$), and $\mathrm{IG}^{\mathrm{o}}_{7,3}$ ($\varepsilon = 8$) were obtained in the Cr,Nd:YAG SQS microchip laser at $P_{\mathrm{in}} = 2.7$, 2.9, 3.3 and 3.5 W, respectively, as shown in figure 2(c).

Compared to the rectangular top-hat transverse profiles obtained in the CW Nd:YAG microchip laser pumped with a tilted pump beam as shown in figure 2(a), the tilted beam pumped Nd:YAG/Cr^{4+}:YAG PQS microchip laser and Cr,Nd:YAG SQS microchip laser oscillated in IG modes, as shown in figures 2(b) and (c). The breaking of the cavity symmetry in the CW Nd:YAG microchip laser under tilted beam pumping is not sufficient to force the CW Nd:YAG microchip laser to oscillate in IG modes. However, IG modes obtained in the tilted beam pumped Nd:YAG/Cr^{4+}:YAG PQS and Cr,Nd:YAG SQS microchip lasers clearly show that the Cr^{4+}:YAG saturable absorber plays a key role in the formation of IG modes in Nd:YAG/Cr^{4+}:YAG PQS and Cr,Nd:YAG SQS microchip lasers. Therefore, the possible IG mode formation mechanism in the tilted beam pumped Nd:YAG/Cr^{4+}:YAG PQS and Cr,Nd:YAG SQS microchip lasers is that the Cr^{4+} saturable absorber acts as the spatial light filter to select the suitable IG modes in the deformed pumped area inside the gain medium. The deformed pump beam area inside the gain medium induced by the tilted beam pumping provides an arena for possible IG mode oscillation selected by the nonlinear absorption of Cr^{4+} ions.

The Cr^{4+} ions saturable absorbers do not only determine the formation of IG modes in the Nd:YAG/Cr^{4+}:YAG PQS and Cr,Nd:YAG SQS microchip lasers, but also have strong effects on the performance of Nd:YAG/Cr^{4+}:YAG PQS and Cr,Nd:YAG SQS microchip lasers. The laser performance of the CW Nd:YAG microchip laser, Nd:YAG/Cr^{4+}:YAG PQS microchip laser and Cr,Nd:YAG SQS microchip laser was measured. Figure 3 shows the output power of the CW Nd:YAG microchip laser and Nd:YAG/Cr^{4+}:YAG PQS microchip laser as a function of P_{in}, together with the output power of the Cr,Nd:YAG SQS microchip laser for comparison. The pump power thresholds of the CW Nd:YAG microchip laser, Nd:YAG/Cr^{4+}:YAG PQS microchip laser, and Cr,Nd:YAG SQS microchip laser are 0.45 W, 0.8 W, and 0.92 W, respectively. The increase in the incident pump power threshold for the Nd:YAG/Cr^{4+}:YAG PQS microchip laser was attributed to the insert losses of the Cr^{4+}:YAG crystal in the laser cavity. The high incident pump power threshold of the Cr,Nd:YAG SQS microchip laser was caused by the severe distortion of crystalline lattices and defects with codoped Cr ions and Nd^{3+} ions in the same host crystal. It is well known that the Nd^{3+} ions in Nd:YAG crystal are formed by substituting the Y^{3+} ions. And it has been demonstrated that the Cr^{4+} ions in Cr^{4+}:YAG crystal are formed by substituting the tetrahedral Al^{3+} sites, compensating charges such as Ca^{2+} or Mg^{2+} ions which are required to substitute the dodecahedral Y^{3+} sites. Because the ionic radii of Nd^{3+} ions and Y^{3+} ions are different, and the ionic radii of Cr ions and Al^{3+} ions are also different, the formation of Nd^{3+} ions and Cr^{4+} ions simultaneously in Cr,Nd:YAG crystal causes aggressive distortion of crystalline lattices and more defects compared to the formation of Nd^{3+} ions in Nd:YAG crystal or Cr^{4+} ions in Cr^{4+}:YAG crystal. And the compensating charges also induce distortion and extra losses in growth of Cr,Nd:YAG crystal. Therefore, for the same doping concentration of Nd^{3+} ions and Cr ions, the defects and distortion in Cr,Nd:YAG crystal are more severe than that in Nd:YAG crystal and Cr^{4+}:YAG crystal. For Nd:YAG, Cr^{4+}:YAG and Cr,Nd:YAG crystals doped with 1 at.% Nd^{3+} ions and 0.01 at.% Cr ions used in the laser experiments, the threshold pump power for the Cr,Nd:YAG SQS microchip laser is higher than for the Nd:YAG/Cr^{4+}:YAG PQS microchip laser. The output power increases linearly with P_{in} for the CW Nd:YAG microchip laser. The slope efficiency (η_{S}) is measured to be 33.2%. The maximum output power of 0.93 W was obtained at $P_{\mathrm{in}} = 3.5$ W, the optical-to-optical efficiency ($\eta_{\mathrm{O\text{–}O}}$) was 27%. The average output power of the Nd:YAG/Cr^{4+}:YAG PQS microchip laser and the Cr,Nd:YAG SQS microchip laser increases linearly with P_{in}. The slope efficiencies (η_{S}) drop to 21.5% and 11.4% for the PQS Nd:YAG microchip laser and Cr,Nd:YAG SQS microchip laser, respectively. The maximum average output power of 0.57 W and 0.31 W was obtained at $P_{\mathrm{in}} = 3.5$ W for the Nd:YAG/Cr^{4+}:YAG PQS microchip laser and the Cr,Nd:YAG SQS microchip laser, respectively. The optical-to-optical efficiencies were 16.3% and 8.8%, respectively. The output power from these three lasers is not saturated and can be further scaled by applying high pump power. The drop of the average output power in the Nd:YAG/Cr^{4+}:YAG PQS microchip laser is attributed to the insert losses of Cr^{4+}:YAG saturable absorber in the laser cavity. The further degraded performance of the Cr,Nd:YAG SQS microchip laser is attributed to severe distortion of the crystalline lattices and defects introduced in codoped Cr,Nd:YAG crystal.

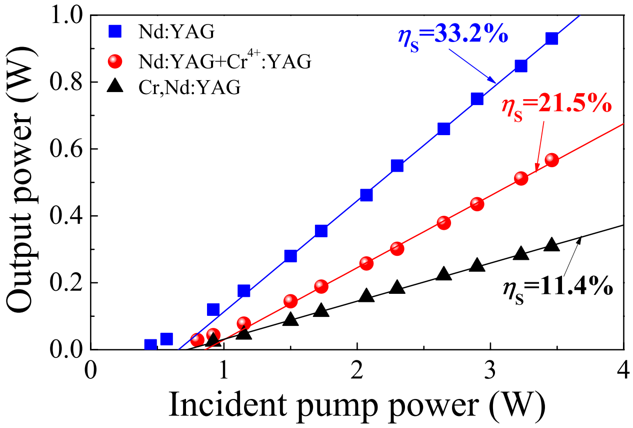

Figure 3. The output power as a function of the incident pump power for the CW Nd:YAG microchip laser, Nd:YAG/Cr^{4+}:YAG PQS microchip laser and Cr,Nd:YAG SQS microchip laser.

The IG modes obtained under the same pumping conditions in the Nd:YAG/Cr^{4+}:YAG PQS microchip laser and the Cr,Nd:YAG SQS microchip laser are different. This is due to the different doping concentration of Cr^{4+} ions and cavity length. The different Cr^{4+} ion doping concentrations determine the different sizes of the Cr^{4+}-ion domains and form different IG modes. At the same time, the different Cr^{4+}-ion domains have a great effect on the laser performance of the

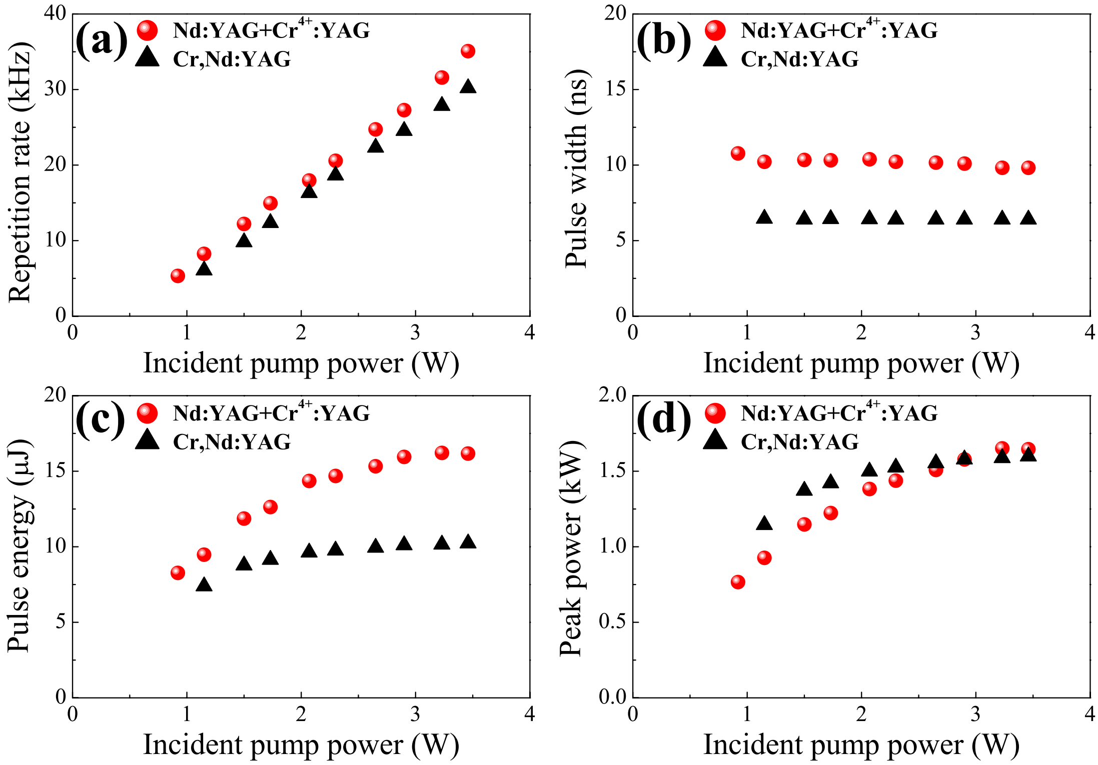

Figure 4. The repetition rate (a), pulse width (b), pulse energy (c) and peak power (d) as a function of the incident pump power.

Nd:YAG/Cr^{4+}:YAG PQS microchip laser and the Cr,Nd:YAG SQS microchip laser. The output pulse characteristics are also affected by factors such as defects of the crystalline lattice and cavity length. The defects and distortion of the crystalline lattice in Cr,Nd:YAG crystal is more severe than in Cr^{4+}:YAG crystal, and degrades the performance of the Cr,Nd:YAG SQS microchip laser. The repetition rate and the pulse energy of the Cr,Nd:YAG SQS microchip laser is less than those obtained in Nd:YAG/Cr^{4+}:YAG PQS microchip laser. The repetition rate increases with P_{in} for both PQS and SQS microchip lasers, as shown in figure 4(a). When P_{in} is 3.5 W, the highest repetition rates of 38.3 kHz and 27.9 kHz were obtained for PQS and SQS microchip lasers, respectively. The maximum pulse energy is about 15 μJ and 10 μJ for PQS and SQS microchip lasers, respectively. In the Nd:YAG/Cr^{4+}:YAG PQS microchip laser, the pulse energy increases slowly with the incident pump power when P_{in} is less than 2.7 W and tends to be saturated with further increase in P_{in}, as shown in figure 4(c). This is caused by the full saturation of the Cr^{4+}:YAG saturable absorber under high intracavity laser intensity at high pump power level, and the energy stored in the Nd:YAG crystal is fully extracted, so the pulse energy remains constant. In the Cr,Nd:YAG SQS microchip laser, the pulse energy remained essentially constant with the increase in P_{in}. It is well known that the pulse width of passively Q-switched lasers is mainly governed by the initial transmission of the saturable absorber and cavity length. For the same initial transmission of the saturable absorber, the shorter the cavity length, the shorter the pulse width that is generated. For the same cavity length, the higher the initial transmission of the saturable absorber, the wider the output pulse. Because the cavity length ($L_C = 1.8$ mm) of the Cr,Nd:YAG SQS microchip laser is shorter than that ($L_C = 3.3$ mm) of the Nd:YAG/Cr^{4+}:YAG PQS microchip laser, and the T_0 for both cases are comparable, the pulse width of the PQS microchip laser is mainly determined by the cavity length. The pulse width of the Cr,Nd:YAG SQS microchip laser is shorter than that of the Nd:YAG/Cr^{4+}:YAG PQS microchip laser. The pulse widths remained substantially constant (10 ns for the Nd:YAG/Cr^{4+}:YAG PQS microchip laser and 6.5 ns for the Cr,Nd:YAG SQS microchip laser) with the increase in P_{in}, as shown in figure 4(b). The short pulse width obtained in the Cr,Nd:YAG SQS microchip laser is beneficial for increasing the peak power of the Cr,Nd:YAG SQS microchip laser. And the peak power of the Cr,Nd:YAG SQS microchip laser is improved with short pulse width. The variation in the peak powers for PQS and SQS microchip lasers with P_{in} is similar to the variation of the pulse energy with P_{in}. The highest peak power of 1.5 kW is achieved for both PQS and SQS microchip lasers, as shown in figure 4(d). Therefore, a short laser cavity in the PQS microchip laser is beneficial for generating short pulses with high peak power. The performance of the Nd:YAG/Cr^{4+}:YAG PQS microchip laser such as short pulse width and high peak power can be further enhanced by applying thin Cr^{4+}:YAG crystal doped with high Cr concentration to decrease initial transmission.

4. Theoretical analysis of forming IG modes in Nd:YAG/Cr^{4+}:YAG PQS microchip laser

Based on the experimental results for the CW Nd:YAG microchip laser, Nd:YAG/Cr^{4+}:YAG PQS microchip laser and

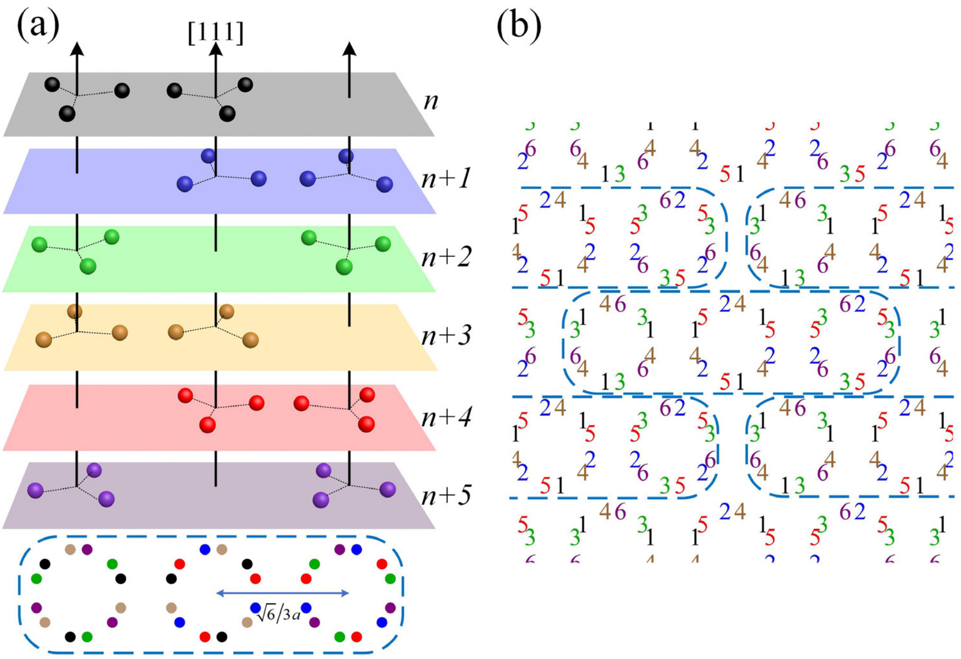

Figure 5. The spatial distribution of the tetrahedral site Al^{3+} ions in a [1 1 1]-cut YAG crystal. (a) The distribution of tetrahedral Al^{3+} sites in six consecutive (1 1 1) planes and the projection of the tetrahedral Al^{3+} sites from six consecutive (1 1 1) planes, each dot representing a tetrahedral Al^{3+} site; (b) the periodical distribution of the projection of the tetrahedral Al^{3+} sites in six different (1 1 1) planes, number *n* representing the *n*th plane where tetrahedral Al^{3+} site is located.

Cr,Nd:YAG SQS microchip laser, the formation of IG modes in microchip lasers under tilted beam pumping is determined by the Cr^{4+} ions saturable absorber. The formation of IG modes in a tilted beam pumped passively Q-switched microchip laser is governed by the interaction between the deformed pump area and the distribution of Cr^{4+} ions. The nonlinear absorption of the Cr^{4+} ions saturable absorber strongly depends on the laser intensity, and the possible oscillation of IG modes in the tilted beam pumped Nd:YAG/Cr^{4+}:YAG PQS microchip laser strongly relies on the intracavity laser intensity distribution. The intracavity laser intensity distribution is determined by the inversion population distribution provided with the pump beam applied on the gain medium. The intracavity laser intensity is proportional to the inversion population provided by the pump power. And the intracavity laser intensity distribution is also strongly affected by the gain saturation effect, thermal lens effect and gain guiding effect. Therefore, the distribution of Cr^{4+} ions in YAG and the deformed pump area inside the gain medium, taking into account the asymmetrical thermal lens effect, should be considered in illustrating the formation of IG modes in PQS microchip lasers.

It is well known that the Cr^{4+}:YAG crystal belongs to the cubic system [29]. In YAG crystal there are two kinds of lattice sites for Al^{3+} ions, the tetrahedral Al^{3+} site and the octahedral Al^{3+} site. The Cr^{4+} ions in YAG crystal are formed by substituting the tetrahedral Al^{3+} sites; compensating charges such as Ca^{2+} or Mg^{2+} ions are required to substitute the dodecahedral Y sites [30]. Owing to the cubic symmetry, the distribution of Cr^{4+} ions in YAG crystal can be considered as the distribution of tetrahedral Al^{3+} sites in YAG crystal. The tetrahedral Al^{3+} ions distribute regularly and uniformly in the (1 1 1) plane of YAG crystal. Therefore, the distribution of Cr^{4+} ions in Cr^{4+}:YAG crystal can be illustrated by stating the distribution of the tetrahedral Al^{3+} ions in YAG crystal. In a (1 1 1) plane of YAG crystal, an equilateral triangle is formed by connecting the adjacent tetrahedral Al^{3+} sites. The distribution of the tetrahedral Al^{3+} sites on the (1 1 1) planes has been studied and it has been found that the relative distribution of the tetrahedral Al^{3+} sites repeats itself every six consecutive (1 1 1) planes. In other words, the location of tetrahedral Al^{3+} sites on the *n*th (1 1 1) plane is consistent with the locations of tetrahedral Al^{3+} sites on the $n + 6$th (1 1 1) plane. Figure 5 shows the distribution of the tetrahedral Al^{3+} sites for six consecutive (1 1 1) planes, each dot in figure 5(a) representing a tetrahedral Al^{3+} site and the number *n* in figure 5(b) representing the *n*th plane where the tetrahedral Al^{3+} site is located. The distance *d* between each two consecutive (1 1 1) planes is $\sqrt{3}a/12$, where *a* is the lattice constant of YAG crystal, so the distance *L* between the *n*th (1 1 1) plane and the $n + 6$th (1 1 1) plane is $\sqrt{3}a/2$. The tetrahedral Al^{3+} sites are periodically distributed in space, and the sites distribution of one cycle is shown in figure 5(a). The adjacent tetrahedral Al^{3+} sites within six (1 1 1) planes form a circular distribution on the projection of the (1 1 1) plane, and the projection of the tetrahedral Al^{3+} sites in the dashed area is taken as one cycle, as shown in figure 5(a). The distance between the centers of adjacent rings is $\sqrt{6}a/3$.

The concentration of Cr^{4+} ions in the Cr^{4+}:YAG crystal is usually determined by measuring the initial transmission of Cr^{4+}:YAG crystal of a certain length. The initial transmission of Cr^{4+}:YAG crystal is related to the Cr^{4+} ion concentration and the length of the Cr^{4+}:YAG crystal, and can be expressed as [31]:

$$T_0 = \exp(-n_0\sigma_{\mathrm{gs}}l_{\mathrm{s}}), \tag{2}$$

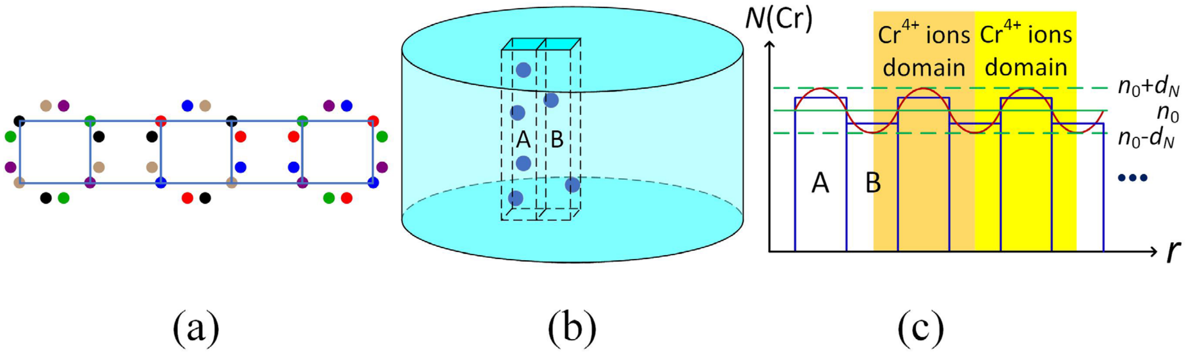

Figure 6. The formation and distribution of the Cr^{4+}-ion domains. (a) The distribution of the projection of the tetrahedral Al^{3+} sites in six different (1 1 1) planes. (b) The number of Cr^{4+} ions in the A and B regions in the Cr^{4+}:YAG crystal, the blue solid dots indicate the Cr^{4+} ions. (c) The trend of Cr^{4+} ion doping concentration along the r axis, where r represents the horizontal axis, N(Cr) represents the doping concentration of Cr^{4+} ions, n_0 indicates the average doping concentration of Cr^{4+} ions in the entire Cr^{4+}:YAG crystal, and d_N represents the fluctuation range of the doping concentration of Cr^{4+} ions.

where n_0 is the total concentration of Cr^{4+} ions in the Cr^{4+}:YAG crystal, σ_{gs} is the ground-state absorption cross-section of Cr^{4+}:YAG crystal, and l_s is the length of the Cr^{4+}:YAG crystal. The total concentration of Cr^{4+} ions in the Cr^{4+}:YAG crystal can be expressed as:

$$n_0 = \frac{-\ln T_0}{\sigma_{gs} l_s}. \quad (3)$$

For the Cr^{4+}:YAG crystal with $T_0 = 95\%$ used in the Nd:YAG/Cr^{4+}:YAG PQS microchip laser, the Cr^{4+} ion concentration, n_0, was estimated to be 7.95×10^{16} cm^{-3} with the parameters of $\sigma_{gs} = 4.3 \times 10^{-18}$ cm^2, and $l_s = 0.15$ cm. It is also known that the total particle density in the YAG crystal is 9.2×10^{22} cm^{-3}, so that there are about 1.16×10^6 ions around one Cr^{4+} ion in Cr^{4+}:YAG crystal under the assumption of uniform distribution of Cr^{4+} ions. We assume that the space occupied by each Cr^{4+} ion is a cube in the case of uniform doping. The distance between any two nearest adjacent Cr^{4+} ions is 2.33×10^{-8} m ($\approx 19a$) under the uniform distribution of Cr^{4+} ions in a Cr^{4+}:YAG crystal with $T_0 = 95\%$.

It is well known that the dimension of a single ion is on the nanometer scale and does not affect the formation of modes. The role of Cr^{4+}:YAG crystal in laser mode selection is caused by the combination of numerous Cr^{4+} ions to form Cr^{4+}-ion domains of a size (micrometers in diameter) comparable to the laser wavelength. Therefore, the formation of Cr^{4+}-ion domains along the laser direction (e.g. ⟨1 1 1⟩ direction) in Cr^{4+}:YAG crystal is proposed for explaining IG mode oscillation in tilted pumped Nd:YAG/Cr^{4+}:YAG PQS microchip lasers. A network along the laser direction is formed with adjacent Cr^{4+}-ion domains in Cr^{4+}:YAG crystal, which acts as a spatial light filter in the formation of IG mode oscillation. Here, the formation of IG modes with Cr^{4+}-ion domains is elucidated. Although the tetrahedral Al^{3+} sites are periodically distributed, they are not evenly spaced with the same interatomic distance. We divide some adjacent regions of the same size on the projection of the (1 1 1) plane, and the number of the tetrahedral Al^{3+} sites is not the same in different regions, as shown in figure 6(a). When the size of the selected region increases, the difference in the number of tetrahedral Al^{3+} sites still exists. This will lead to different amounts of Cr^{4+} ions doped in different regions in the Cr^{4+}:YAG crystal. As shown in figure 6(b), the number of doped Cr^{4+} ions in the A and B regions will be different in the Cr^{4+}:YAG crystal, which causes different modulation of the laser in the A and B regions. When we select two adjacent regions of the same size (20 μm × 20 μm × 1.5 mm) in the Cr^{4+}:YAG crystal, the number of tetrahedral Al^{3+} sites in the two regions differs by approximately 5.8×10^{10}, by numerical calculation. This indicates that the amount of doped Cr^{4+} ions will be different in different regions of the Cr^{4+}:YAG crystal. As shown in figure 6(c), the abscissa indicates the r-axis in the horizontal direction, and the ordinate N(Cr) indicates the doping concentration of Cr^{4+} ions. The average doping concentration of Cr^{4+} ions in region A is higher than that in region B, and the change is periodic along the r axis, where n_0 indicates the average doping concentration of Cr^{4+} ions in the entire Cr^{4+}:YAG crystal, and d_N represents the fluctuation range of the doping concentration of Cr^{4+} ions. When the amount of doped Cr^{4+} ions is fixed, if the average doping concentration of Cr^{4+} ions in one region is high, there would be a region with a lower doping concentration of Cr^{4+} ions around this region. As we reduce the size of the selected region, the change in Cr^{4+} ion doping concentration along the r-axis will periodically change continuously, as shown by the red curve in figure 6(c). We define the region with a high concentration of Cr^{4+} ions as a Cr^{4+}-ions domain, shown in figure 6(c). When the Cr^{4+}-ions domain reaches the order of micrometers in size (here the size of the Cr^{4+}-ion domain is about 40 μm × 40 μm × 1.5 mm), it will have a modulation effect on the formation of the laser mode. Although the difference in Cr^{4+} ion concentration among the Cr^{4+}-ion domains and surrounding area is small, it is enough to control the loss of different laser modes in the cavity. And the nonlinear saturable absorption of these Cr^{4+}-ion domains plays a key role in the formation of IG laser modes in the Nd:YAG/Cr^{4+}:YAG PQS microchip lasers under tilted pumping.

The Cr^{4+}-ion domains formed in Cr^{4+}:YAG crystal work as a spatial light filter and determine the gain and loss distribution in the intracavity laser. At the same time, the formation of the laser modes is also affected by the pump beam shape and pump area. Besides the shape and incident angle of the

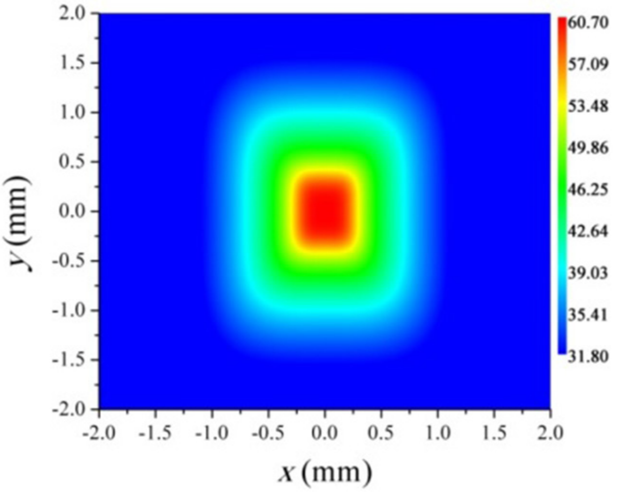

Figure 7. The temperature distribution in the cross section of the crystal.

pump beam, the thermal lens effect of the crystal induced by the thermal loading is also affected by the pump area for possible laser mode oscillation. The steady state temperature distribution in the Nd:YAG crystal for an end-pumped Nd:YAG/Cr^{4+}:YAG PQS microchip laser can be expressed as [32, 33]

$$\frac{1}{r}\frac{\partial}{\partial r}\left(r\frac{\partial T(r,z)}{\partial r}\right)+\frac{\partial^2 T(r,z)}{\partial z^2}=-\frac{1}{k_c}q(r,z), \tag{4}$$

where the heat source from the pump power can be described as a super-Gaussian shaped distribution of the pump beam

$$q(r,z)=\frac{2\eta_{\mathrm{h}}P_{\mathrm{in}}\alpha}{\pi w_{\mathrm{p}}^2}\exp\left(-\frac{2r^4}{w_{\mathrm{p}}^4}\right)\exp(-\alpha z), \tag{5}$$

where α is the absorption coefficient of Nd:YAG crystal, η_{h} is the heat transfer coefficient, P_{in} is the incident pump power, k_{c} is the heat conduction constant, w_{p} is the radius of the pump beam.

The spatial temperature distribution inside the Nd:YAG crystal under the single emitter laser diode pumping is calculated according to equation (4). The material parameters of Nd:YAG crystal used in the calculation are $\alpha = 7.8\,\mathrm{cm}^{-1}$, $\eta_{\mathrm{h}} = 0.32$, $k_{\mathrm{c}} = 0.014$ W (mm · K)$^{-1}$, $l = 1.8\,\mathrm{mm}$, and the incident pump power is $P_{\mathrm{in}} = 2.9$ W. Figure 7 shows the temperature distribution in the cross section of the crystal when $z = 0$, the highest temperature is about 60.7 °C at the center of the crystal, and the temperature is about 31.8 °C at the edge of the crystal. Since the temperature in Nd:YAG crystal exhibits a gradient change in the horizontal direction (x) and the vertical direction (y), it inevitably leads to a gradient change for the focal length (f_{t}) of the thermal lens. The f_{t} gradually increases from the central area to the edge area along the horizontal direction or the vertical direction. The temperature gradient in the horizontal direction is higher than the temperature gradient in the vertical direction, so the f_{t} in the horizontal direction is smaller than the thermal lens focal length in the vertical direction. Therefore, the focus effect of the pump spot in the horizontal direction will be significantly stronger than the focus effect in the vertical direction.

The center axis of the resonator is taken as the z-axis to establish the Cartesian coordinate (x, y, z). The tilted pump beam from the single emitter laser diode can be expressed as

$$E(x,y,z)=E_0\cdot\exp\left[-\left(\frac{x^4}{w_x(z\cos(\theta)+y\sin(\theta))^4}+\frac{[-z\sin(\theta)+y\cos(\theta)]^4}{w_y(z\cos(\theta)+y\sin(\theta))^4}\right)\right], \tag{6}$$

where θ denotes the incident angle of the pump beam at the rear cavity mirror of this resonator.

When the thermal lens effect of the Nd:YAG crystal is taken into account, the propagation of the pump beam in the cavity is affected. The contraction factors $\beta_x(y)$ and $\beta_y(x)$ have been introduced to describe the effect of the thermal lens induced by the pump beam along the horizontal and vertical directions, and $w_x(z)$ and $w_y(z)$ can be modified as

$$w_x(z)=\sqrt{w_{0x}^2\left[1+\frac{\beta_x(y)(M_x^2)^2\lambda_{\mathrm{p}}^2z^2}{\pi^2w_{0x}^4n^4}\right]}, \tag{7}$$

$$w_y(z)=\sqrt{w_{0y}^2\left[1+\frac{\beta_y(x)\left(M_y^2\right)^2\lambda_{\mathrm{p}}^2z^2}{\pi^2w_{0y}^4n^4}\right]}, \tag{8}$$

where w_{0x} and w_{0y} are the focused pump beam waists along the x-axis and y-axis, respectively, n is the refractivity of the laser crystal, M_x^2 and M_y^2 are the beam quality factors in the x-direction and the y-direction, respectively, λ_p is the wavelength of the pump beam. In addition, $\beta_x(y) \leqslant 1$ and $\beta_y(x) \leqslant 1$. The thermal lens has no effect on the laser beam when $\beta_x(y)$ and $\beta_y(x)$ are equal to one.

Because the thermal lens effect induced by the pump power does not only affect the pump beam and laser beam propagation inside the gain medium, but also has a great effect on the distribution of the inversion populations, the inversion population distribution inside the Nd:YAG crystal is calculated theoretically by introducing the gradient thermal lens effect along the x and y directions. The thermal lens dependent inversion populations can be represented as

$$\Delta N(x,y,z)=\frac{2P_{\mathrm{in}}\alpha f_{\mathrm{a}}\tau}{h\nu_{\mathrm{p}}\pi w_x(z_1)w_y(z_1)}\cdot\exp\left[-2\left(\frac{x_1^4}{\omega_x(z_1)^4}+\frac{y_1^4}{\omega_y(z_1)^4}\right)\right]\cdot\exp\left[-\alpha\frac{z}{\cos(\theta)}\right], \tag{9}$$

and

$$\begin{cases}x_1=x\\ y_1=-z\sin(\theta)+y\cos(\theta)\\ z_1=z\cos(\theta)+y\sin(\theta)\end{cases}, \tag{10}$$

where f_{a} is the fractional equilibrium Boltzmann population of the upper laser level in the crystal field component (one for a four-level system), τ is the fluorescence lifetime of the gain crystal, h denotes the Planck constant, ν_{p} is the frequency of the pump beam.

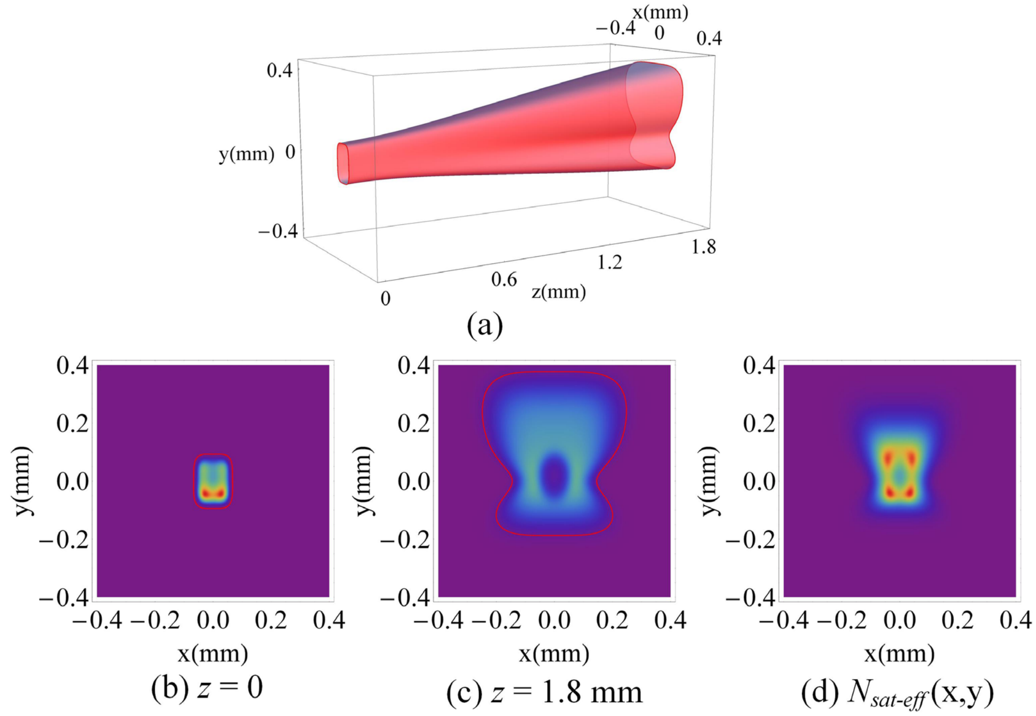

(a)

(b) $z = 0$

(c) $z = 1.8$ mm

(d) $N_{sat\text{-}eff}$(x,y)

Figure 8. The distribution of the saturated inversion populations induced by the gradient thermal lens effect along fast-axis and slow-axis of the single-emitter laser diode. (a) The $N_{\text{sat}} = N_{\text{i}}$ contour surface inside the Nd:YAG crystal; (b) distribution of the saturated inversion population at $z = 0$; (c) distributions of the saturated inversion population at $z = 1.8$ mm, the red solid lines represents $N_{\text{sat}} = N_{\text{i}}$ contour lines; (d) Effective saturated inversion population distribution along the thickness of Nd:YAG crystal.

The saturated inversion population under the high laser intensity is given by [22]:

$$N_{\text{sat}}(x,y,z) = \Delta N(x,y,z)/[1 + I(x,y,z)/I_{\text{sat}}], \quad (11)$$

where $I(x, y, z)$ is the intensity of the laser mode inside the laser resonator and I_{sat} is the laser saturation intensity of the laser crystal.

The initial inversion population of the Nd:YAG/Cr^{4+}:YAG PQS laser under CW pumping can be written as [22]

$$N_{\text{i}} = [2\sigma_{\text{gs}}N_{\text{s0}}l_{\text{s}} + \ln(1/R_{\text{oc}}) + \delta_{\text{Loss}}]/(2\sigma l), \quad (12)$$

where σ is the emission cross section of gain medium, N_{s0} is the total concentration of Cr^{4+} in the Cr^{4+}:YAG, l is the length of the Nd:YAG crystal, l_{s} is the length of the Cr^{4+}:YAG crystal, R_{OC} is the reflectivity of the output coupler, and δ_{Loss} is the total intracavity loss.

Figure 8 shows the theoretically calculated saturated inversion population distributions inside the Nd:YAG crystal in the Nd:YAG/Cr^{4+}:YAG PQS microchip laser under tilted pumping when the gradient thermal lens effect along the x-direction and the y-direction are taken into account. The pump beam focus spot is located on the rear surface of the Nd:YAG crystal ($z = 0$). The parameters used in the theoretical calculation are as follows: $\sigma = 2.8 \times 10^{-19}$ cm^2, $\sigma_{\text{gs}} = 4.3 \times 10^{-18}$ cm^2, $l = 1.8$ mm, $l_{\text{s}} = 1.5$ mm, $N_{\text{s0}} = 4.89 \times 10^{16}$ cm^{-3}, $R_{\text{oc}} = 95\%$, $P_{\text{in}} = 2.9$ W, $\alpha = 7.8$ cm^{-1}, $\theta = 3°$, $\delta_{\text{Loss}} = 0.1$, $\tau = 230$ μs. Figure 8(a) gives the 3D saturated inversion population distribution inside the Nd:YAG crystal when the saturated inversion population is equal to the initial inversion population of the Nd:YAG/Cr^{4+}:YAG PQS microchip laser. The saturated inversion population distribution gives the possible laser mode area inside the resonator. Due to the influence of the thermal lens with gradient focal length, the divergence angle of the pump beam at different positions is different, and the divergence angle of the pump beam at the center position is smaller than the divergence angle of the pump beam at the periphery. The distributions of the saturated inversion populations at $z = 0$ and $z = 1.8$ mm are shown in figures 8(b) and (c), respectively. Inside the Nd:YAG crystal, the distribution area of the saturated inversion population gradually increases along the thickness, while the saturated inversion population density gradually decreases owing to the exponential decay of the absorbed pump power. The saturated inversion population distribution on any cross sections along the thickness of Nd:YAG crystal cannot be used to accurately analyze the formation of laser modes. To reflect the overall effect, we define the effective saturated inversion population distribution to represent the average distribution of saturated inversion population in the cavity. When the length of the laser crystal is l, the effective saturated inversion population is expressed as

$$N_{\text{sat-eff}}(x,y) = \int_0^l N_{\text{sat}}(x,y,z)dz/l. \quad (13)$$

The effective saturated inversion population is calculated, as shown in figure 8(d). The inversion populations in the central region are significantly contracted inward in the horizontal direction, and the contraction amplitude gradually decreases from the center to both sides. This provides a favorable gain region for generating the IG mode.

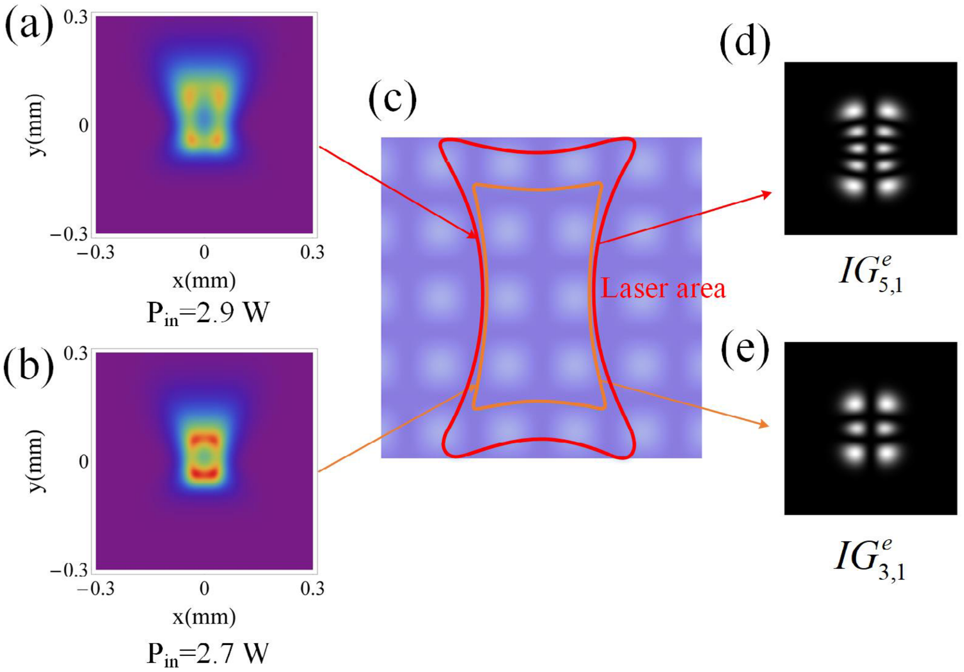

Figure 9. Spatial modulation effect of Cr^{4+}-ion domains on selecting IG modes for Nd:YAG/Cr^{4+}:YAG PQS microchip laser at different pump powers. (a) Effective saturated inversion population distribution at $P_{in} = 2.9$ W; (b) effective saturated inversion population distribution at $P_{in} = 2.7$ W; (c) distribution of the Cr^{4+}-ion domains along [1 1 1] direction; (d) $IG^e_{5,1}$ mode obtained at $P_{in} = 2.9$ W; (e) $IG^e_{3,1}$ mode obtained at $P_{in} = 2.7$ W.

In order to illustrate the spatial selection of IG mode oscillation in the Nd:YAG/Cr^{4+}:YAG PQS microchip laser by the Cr^{4+}-ion domains as a spatial filter, $IG^e_{5,1}$ mode and $IG^e_{3,1}$ mode are taken as examples (see figure 2). Figures 9(a) and (b) show the effective saturated inversion population distribution at $P_{in} = 2.9$ W and 2.7 W, respectively. The effective saturated inversion population density increases with the increase in pump power, and makes possible the laser area increase. The distribution of the Cr^{4+}-ions domain along the [1 1 1] direction is shown in figure 9(c). Each bright spot represents a Cr^{4+}-ion domain of about 40 μm × 40 μm and the area surrounded by red curves in figure 9(c) represents the laser oscillation region at $P_{in} = 2.9$ W. When the Cr^{4+}-ions domain is formed in the order of micrometers in size, it will have a significant spatial modulation effect on the formation of the laser mode. There are ten Cr^{4+}-ion domains in the laser oscillation region, and these domains have a nonlinear saturated absorption for the intracavity laser, the laser energy is stored in this areas until the saturable absorber is bleached and laser pulses with selected laser mode are generated, and the laser pattern ($IG^e_{5,1}$) shown in figure 9(d) is obtained. When the P_{in} drops to 2.7 W, the laser oscillation region surrounded by orange curves in figure 9(c) decreases significantly. This is due to the decline in the saturated inversion population. There are only six Cr^{4+}-ion domains in the laser oscillation region, and the order of the laser mode is significantly reduced, $IG^e_{3,1}$ mode is obtained in the PQS microchip laser, as shown in figure 9(e). At low pump power, the pump area is generally larger than the actual laser oscillation region, however, when P_{in} is high, the laser oscillation region may be equal to or larger than the size of the pump region due to the gain guidance effect, and the higher order IG mode will be generated.

For the Cr,Nd:YAG SQS microchip laser with $T_0 = 94\%$, the Cr^{4+} ion concentration was estimated to be 7.99 × 10^{16} cm^{-3}, which is comparable to that of the Nd:YAG/Cr^{4+}:YAG PQS microchip laser with $T_0 = 95\%$. A 1.8 mm-thick Cr,Nd:YAG crystal is longer than the 1.5 mm-thick Cr^{4+}:YAG used in the Nd:YAG/Cr^{4+}:YAG PQS microchip laser. This indicates that for the same amount of Cr ions doped in the Cr,Nd:YAG crystal and Cr^{4+}:YAG crystal, the modulation depth and losses introduced in the Cr,Nd:YAG microchip laser is high. Therefore, the order of the IG laser modes generated in the Cr,Nd;YAG SQS microchip laser is lower than that obtained in the Nd:YAG/Cr^{4+}:YAG PQS microchip lasers under the same pump power. Also, the pump power threshold of the Cr,Nd:YAG SQS microchip laser is higher than that of the Nd:YAG/Cr^{4+}:YAG PQS microchip laser. The performance of the Cr,Nd:YAG SQS microchip laser is degraded compared to that of the Nd:YAG/Cr^{4+}:YAG PQS microchip laser.

5. Conclusion

The formation of IG modes in tilted beam pumped Nd:YAG/Cr^{4+}:YAG PQS and Cr,Nd:YAG SQS microchip lasers has been investigated experimentally and theoretically. The interaction of the Cr^{4+} ion distribution in YAG crystal and the deformed laser beam induced by the thermal lens is attributed to the formation of IG modes in passively Q-switched microchip lasers. The asymmetric saturated inversion population distributions inside the gain medium are responsible for a platform that forms IG modes with Cr^{4+}-ion domains as the spatial light filter. The inversion population is selectively saturated by the Cr^{4+}-ion domains when the laser intensity is high enough, which makes the Nd:YAG/Cr^{4+}:YAG PQS microchip laser oscillate in IG modes. The work shows a clear image of IG mode oscillation in the Nd:YAG/Cr^{4+}:YAG PQS microchip laser under tilted beam pumping. The controllable IG modes could be obtained by carefully selecting the pump beam distribution and modulation depth of Cr^{4+}:YAG crystal in the Nd:YAG/Cr^{4+}:YAG PQS microchip laser.

Acknowledgment

This work was supported by the National Natural Science Foundation of China (61475130 and 61275143), the Program for New Century Excellent Talents in University (NCET-09-0669) and the Fundamental Research Funds for Xiamen University (20720162005).

References

[1] Woerdemann M, Alpmann C and Denz C 2011 Optical assembly of microparticles into highly ordered structures using Ince–Gaussian beams *Appl. Phys. Lett.* **98** 111101
[2] Woerdemann M, Alpmann C, Esseling M and Denz C 2013 Advanced optical trapping by complex beam shaping *Laser Photonics Rev.* **7** 839–54
[3] Kuo C F and Chu S C 2013 Numerical study of the properties of optical vortex array laser tweezers *Opt. Express* **21** 26418–31
[4] Ohtomo T, Chu S C and Otsuka K 2008 Generation of vortex beams from lasers with controlled Hermite- and Ince–Gaussian modes *Opt. Express* **16** 5082–94
[5] Schwarz U T, Bandres M A and Gutierrez-Vega J C 2004 Observation of Ince–Gaussian modes in stable resonators *Opt. Lett.* **29** 1870–2
[6] Ohtomo T, Kamikariya K, Otsuka K and Chu S C 2007 Single-frequency Ince–Gaussian mode operations of laser-diode-pumped microchip solid-state lasers *Opt. Express* **15** 10705–17
[7] Otsuka K, Nemoto K, Kamikariya K, Miyasaka Y and Chu S C 2007 Linearly polarized single-frequency oscillations of laser-diode-pumped microchip ceramic Nd: YAG lasers with forced Ince–Gaussian mode operations *Japan. J. Appl. Phys.* **46** 5865–7
[8] Dong J, Ma J, Ren Y Y, Xu G Z and Kaminskii A A 2013 Generation of Ince–Gaussian beams in highly efficient, nanosecond Cr, Nd:YAG microchip lasers *Laser Phys. Lett.* **10** 085803
[9] Dong J, He Y, Zhou X and Bai S C 2016 Highly efficient, versatile, self-Q-switched, high-repetition-rate microchip laser generating Ince–Gaussian modes for optical trapping *Quantum Electron.* **46** 218–22
[10] He H S, Zhang M M, Dong J and Ueda K I 2016 Linearly polarized pumped passively Q-switched Nd:YVO_4 microchip laser for Ince–Gaussian laser modes with controllable orientations *J. Opt.* **18** 125202
[11] Bentley J B, Davis J A, Bandres M A and Gutierrez-Vega J C 2006 Generation of helical Ince–Gaussian beams with a liquid-crystal display *Opt. Lett.* **31** 649–51
[12] Ngcobo S, Litvin I, Burger L and Forbes A 2013 A digital laser for on-demand laser modes *Nat. Commun.* **4** 2289
[13] Aguirre-Olivas D, Mellado-Villasenor G, Sanchez-de-la-Llave D and Arrizon V 2015 Efficient generation of Hermite–Gauss and Ince–Gauss beams through kinoform phase elements *Appl. Opt.* **54** 8444–52
[14] Ren Y X, Fang Z X, Gong L, Huang K, Chen Y and Lu R D 2015 Dynamic generation of Ince–Gaussian modes with a digital micromirror device *J. Appl. Phys.* **117** 133106
[15] Chu S C 2007 Numerical study for selective excitation of Ince–Gaussian modes in end-pumped solid-state lasers *Opt. Express* **15** 16506–19
[16] Malyutin A A 2007 Modes of a plano-spherical laser resonator with the Gaussian gain distribution of the active medium *Quantum Electron.* **37** 299–306
[17] Kim D J, Mackenzie J I and Kim J W 2016 Adaptable beam profiles from a dual-cavity Nd:YAG laser *Opt. Lett.* **41** 1740–3
[18] Lei J, Hu A, Wang Y and Chen P 2014 A method for selective excitation of Ince–Gaussian modes in an end-pumped solid-state laser *Appl. Phys.* B **117** 1129–34
[19] Ito A, Kozawa Y and Sato S 2010 Generation of hollow scalar and vector beams using a spot-defect mirror *J. Opt. Soc. Am.* A **27** 2072–7
[20] Sato T, Kozawa Y and Sato S 2015 Transverse-mode selective laser operation by unicursal fast-scanning pumping *Opt. Lett.* **40** 3245–8
[21] Zhang M M, He H S and Dong J 2017 Decentered Gaussian beam pumped highly efficient passively Q-switched microchip laser for controllable high-order transverse modes *IEEE Photonics J.* **9** 1501214
[22] Dong J, Bai S C, Liu S H, Ueda K I and Kaminskii A A 2016 A high repetition rate passively Q-switched microchip laser for controllable transverse laser modes *J. Opt.* **18** 055205
[23] Han S, Liu Y Q, Zhang F, Zhou Y, Wang Z P and Xu X G 2015 Direct generation of subnanosecond Ince–Gaussian modes in microchip laser *IEEE Photonics J.* **7** 4500206
[24] Sooy W R 1965 The natural selection of modes in a passive Q-switched laser *Appl. Phys. Lett.* **7** 36–7
[25] Chandonnet A, Piche M and McCarthy N 1990 Beam narrowing by a saturable absorber in a Nd:YAG laser *Opt. Commun.* **75** 123–8
[26] Ishaaya A A, Davidson N and Friesem A A 2005 Very high-order pure Laguerre-Gaussian mode selection in a passive Q-switched Nd: YAG laser *Opt. Express* **13** 4952–62
[27] Chen X M, Bai Y, Jiang M, Li L F, Zhou Y X, Wang H, Ren Z Y and Bai J T 2012 Formation of four phase-locked gaussian beams by saturable absorber in a neodymium-doped yttrium aluminum garnet laser *Appl. Phys. Express* **5** 122701
[28] Dong J, Wang G Y and Cheng Y 2013 Highly efficient passively Q-switched Yb:YAG microchip lasers under high intensity laser-diode pumping *Laser Phys.* **23** 035802
[29] Eilers H, Dennis W M, Yen W M, Kuck S, Peterman K, Huber G and Jia W 1993 Performance of a Cr:YAG laser *IEEE J. Quantum Electron.* **29** 2508–12
[30] Markgraf S A, Pangborn M F and Dieckmann R 1997 Influence of different divalent co-dopants on the Cr^{4+} content of Cr-doped $Y_3Al_5O_{12}$ *J. Cryst. Growth* **180** 81–4
[31] Burshtein Z, Blau P, Kalisky Y, Shimony Y and Kokta M R 1998 Excited-state absorption studies of Cr^{4+} ions in several garnet host crystals *IEEE J. Quantum Electron.* **34** 292–9
[32] Xie W J, Kwon Y, Hu W T and Zhou F 2003 Thermal modeling of solid state lasers with super-Gaussian pumping profiles *Opt. Eng.* **42** 1787–94
[33] Brickus D and Dement'ev A S 2017 Modeling of thermal lensing in a [1 1 1]-cut Nd: YAG rod with temperature-dependent parameters and different pumping profiles *Laser Phys.* **27** 055002